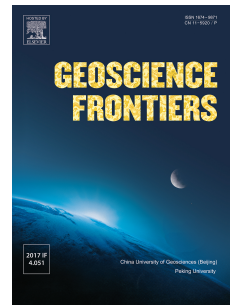


# Journal Pre-proof

Deep mantle hydrogen in the pyrite-type FeO<sub>2</sub>-FeO<sub>2</sub>H system

Qingyang Hu, Jin Liu



PII: S1674-9871(20)30096-7

DOI: <https://doi.org/10.1016/j.gsf.2020.04.006>

Reference: GSF 993

To appear in: *Geoscience Frontiers*

Received Date: 28 October 2019

Revised Date: 2 February 2020

Accepted Date: 12 April 2020

Please cite this article as: Hu, Q., Liu, J., Deep mantle hydrogen in the pyrite-type FeO<sub>2</sub>-FeO<sub>2</sub>H system, *Geoscience Frontiers*, <https://doi.org/10.1016/j.gsf.2020.04.006>.

This is a PDF file of an article that has undergone enhancements after acceptance, such as the addition of a cover page and metadata, and formatting for readability, but it is not yet the definitive version of record. This version will undergo additional copyediting, typesetting and review before it is published in its final form, but we are providing this version to give early visibility of the article. Please note that, during the production process, errors may be discovered which could affect the content, and all legal disclaimers that apply to the journal pertain.

© 2020 China University of Geosciences (Beijing) and Peking University. Production and hosting by Elsevier B.V. All rights reserved.

1   **Deep mantle hydrogen in the pyrite-type FeO<sub>2</sub>-FeO<sub>2</sub>H system**

2   Qingyang Hu\*, Jin Liu

3   Center for High Pressure Science and Technology Advanced Research (HPSTAR),  
4   Beijing, 100094, China.

5

6   \*Corresponding author.

7   *E-mail address:* [qingyang.hu@hpstar.ac.cn](mailto:qingyang.hu@hpstar.ac.cn) (Q. Hu)

8

9

10   **Abstract**

11   Pyrite-type FeO<sub>2</sub> and FeO<sub>2</sub>H were synthesized at the pressure-temperature  
12   conditions relevant to Earth's deep lower mantle. Through the water-iron  
13   reaction, the pyrite-phase is a good candidate to explain the chemical  
14   heterogeneities and seismological anomalies at the bottom of the mantle. The  
15   solid solution of pyrite-type FeO<sub>2</sub> and FeO<sub>2</sub>H, namely the FeO<sub>2</sub>H<sub>x</sub> (0≤x≤1), is  
16   particularly interesting and introduces puzzling chemical states for both the O  
17   and H atoms in the deep mantle. While the role of H in the FeO<sub>2</sub>-FeO<sub>2</sub>H system  
18   has been primarily investigated, discrepancies remain. In this work, we  
19   summarize recent progress on the pyrite-phase, including FeO<sub>2</sub>, FeO<sub>2</sub>H, and  
20   FeO<sub>2</sub>H<sub>x</sub>, which is critical for understanding the water cycling, redox equilibria,  
21   and compositional heterogeneities in the deep lower mantle.

22

23   **Keywords:**

24   Deep lower mantle, Core-mantle boundary, Pyrite-type phase, Hydrogen-bearing  
25   phase

26

27

**28 1. Introduction**

29 Recent high-pressure experiments revealed that major rock-forming elements like Fe  
30 and O exhibit a much richer stoichiometry when pressure is elevated to a few tens of  
31 gigapascals (GPa) ( Lavina et al., 2011; Lavina and Meng, 2015; Merlini et al., 2015;  
32 Bykova et al., 2016; Sinmyo et al., 2016). Weerasinghe et al. (2015) predicted that  
33 pyrite-type (Py)  $\text{FeO}_2$  represents an O-rich composition in the Fe-O binary system.  
34 The high-pressure phase was synthesized experimentally at pressures above 75 GPa,  
35 which is equivalent to the depths of 1800–2900 km, defined as Earth’s deep lower  
36 mantle (DLM) (Hu et al., 2016). An exotic property of the Py- $\text{FeO}_2$  phase is the  
37 ability to associate the structure with light elements like H and He. The incorporation  
38 of those light elements in the lattice expands the pyrite-phase into ternary  
39 compositions like  $\text{FeO}_2\text{H}$  (Hu et al., 2017a; Nishi et al., 2017; Huang et al., 2019) and  
40  $\text{FeO}_2\text{He}$  (Zhang et al., 2018a). Consequently, they are predicted to be candidate  
41 structures to store volatile light elements in Earth’s deep interior.

42  
43 The  $\text{FeO}_2$ - $\text{FeO}_2\text{H}$  system holds the key to a better understanding of deep hydrogen  
44 cycling. While the major components of the lower mantle are made of nominally  
45 anhydrous minerals, Py- $\text{FeO}_2\text{H}$  is among the few recently-discovered deep hydrous  
46 phases (DHPs), including  $\delta$ -AlOOH (Tsuchiya et al., 2002), ultrahydrous stishovite  
47 (Lin et al., 2020), phase H (Nishi et al., 2018), the HH-phase ( $\text{Al},\text{Fe}\text{OOH}$  (Zhang et  
48 al., 2018b), and their solid solutions (Nishi et al., 2019; Ohtani, 2019; Xu et al., 2019).  
49 Intriguingly, the Py- $\text{FeO}_2\text{H}$  is reported to release a portion of hydrogen to form the  
50 solid solution of  $\text{FeO}_2\text{H}_x$  ( $0 \leq x \leq 1$ ) (Hu et al., 2017; Zhu et al., 2017). Dehydrogenation  
51 is different from dehydration in chemistry, and it distinguishes Py- $\text{FeO}_2\text{H}_x$  from the  
52 other DHPs, which usually undergo dehydration at high temperatures ( $T$ ). At shallow  
53 depths, a similar dehydrogenation process also takes place in Fe-bearing amphiboles  
54 upon heating (Hu et al., 2018), coupled with the oxidation of  $\text{Fe}^{2+}$  to  $\text{Fe}^{3+}$ . In contrast,  
55 spectroscopic measurements suggest the dehydrogenation of Py- $\text{FeO}_2\text{H}_x$  does not  
56 result from iron redox and could promote interactions between oxygen atoms to form  
57 peroxide dimers (Boulard et al., 2019; Liu et al., 2019). During a H release process,  
58 the redox state of the pyrite-type  $\text{FeO}_2$ - $\text{FeO}_2\text{H}$  system changes at the same time.  
59 Compared to dehydration, dehydrogenation not only separates H from the DHP  
60 carriers, but also suggests that such novel lower-mantle chemistry may involve a full  
61 suite of elements like O, H, and Fe.

62

63 In this work, we summarize and review previous findings on the Py-phase FeO<sub>2</sub>-  
 64 FeO<sub>2</sub>H system. We start with a brief introduction of the experimental methods using  
 65 the diamond anvil cell (DAC). Then, information on the Py-phase is presented in the  
 66 order of crystal structure, equation of states as a function of *P-T*, and variance of *x* by  
 67 pressurization rates. The major impacts of the Py-phase in the redox equilibria and  
 68 material cycling in Earth's interiors are discussed in the last chapter.

69

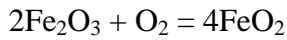
## 70 **2. Experimental methods**

71 Exploring mineral properties under DLM conditions raises many technical challenges.  
 72 Other than a multi anvil equipped with the sintered diamond anvils(Ito et al., 2010),  
 73 the most popular instrument to achieve both high *P* and high *T* at static conditions is  
 74 the diamond anvil cell (DAC)(Fig. 1)(Jephcoat et al., 1987). Diamond anvil culets are  
 75 usually beveled in low angles of 8–10 degrees, with a tip diameter below 150 µm to  
 76 reach above megabar pressures. Consequently, the sample's size is only tens of  
 77 microns. The small sample size requires the use of synchrotron radiation-generated x-  
 78 ray probes for studying the structural, electronic, and seismic properties over megabar  
 79 pressures.

80

81 Approaching mantle geothermal *T* (*e.g.*, >2000 K) under high-*P* often involves the  
 82 use of laser heating (Fig. 1)(Heinz and Jeanloz, 1984). However, the small laser focus  
 83 point and high heat-dissipating rate inevitably generate large temperature gradients.  
 84 Even with double-sided laser heating, which attempts to minimize gradients towards  
 85 the beam axial direction, temperature uncertainties along the radial directions of the  
 86 DAC are still as much as a few hundreds of kelvins (Meng et al., 2015). A good  
 87 sample assembly in such a DAC experiment contains a pre-compressed sample  
 88 platelet, good thermal insulation surrounding the sample, and an auxiliary pressure  
 89 calibrant. Inert gas is among the most popular thermal insulators, which also serves as  
 90 a pressure medium, and can safely heat to ~2600 K at above 80 GPa (Santamaría-  
 91 Pérez et al., 2010). The pressure media can also be a part of the sample assembly,  
 92 particularly for experiments mimicking chemical reactions. For example, Py-FeO<sub>2</sub>  
 93 was initially synthesized from hematite and an oxygen media (Hu et al., 2016) to  
 94 implement the following chemistry:

95



96 Since oxygen becomes a metal above 96 GPa and no longer insulates heat (Akahama  
97 et al., 1995), laser heating was only performed around or below 90 GPa. The auxiliary  
98 pressure calibrant provides robust pressure calibration when ruby fluorescence  
99 becomes weak (Mao et al., 1986). Typically, such calibrants are cubic-structured  
100 metal like Pt and Au, whose equation of states (EOS) are well-calibrated to megabar  
101 pressures (Fei et al., 2007).

102

103 To date, the synthesis and characterization of the pyrite-type FeO<sub>2</sub>-FeO<sub>2</sub>H system  
104 have been performed in such a laser-heated DAC platform. The platform is generally  
105 robust up to 140 GPa and 3300 K, close to the *P-T* conditions found at Earth's core-  
106 mantle boundary. The wide *P-T* range enables scientists to study the crystal structure,  
107 Fe-O-H ternary composition, equation of state, and many other physical properties of  
108 the Py-phase, which are illustrated in the following sections.

109

### 110 **3. Crystal structure**

111 The crystal structures of pyrite-type FeO<sub>2</sub> and FeO<sub>2</sub>H are stable only at high pressures  
112 (*e.g.*, > 75 GPa). While experiments on the variation of H in the FeO<sub>2</sub>-FeO<sub>2</sub>H system  
113 will be discussed in the next session, the fundamental reasoning of such H variation  
114 may stem from the archetypal pyrite structure (Fig. 2). For example, Py-FeO<sub>2</sub> was  
115 synthesized with Fe<sub>2</sub>O<sub>3</sub> and O<sub>2</sub> at 76 GPa and 1800 K (Hu et al., 2016; Zhu et al.,  
116 2019). The cubic unit cell takes the pyrite FeS<sub>2</sub> as a prototype, although the longer O-  
117 O bonding has raised some concerns. For instance, unlike typical peroxides that  
118 features short O-O bonds (usually < 1.5 Å)(Hoffman et al., 1959), Py-FeO<sub>2</sub> features  
119 O-O 1.7–2.2 Å from powder or single-crystal refinements (Koemets et al., 2019; Liu  
120 et al., 2019). With this longer O-O bond, H is able to insert into the middle of two O  
121 atoms and form symmetric H-bonds (Fig. 2)(Nishi et al., 2017). Theoretically, if we  
122 construct an energy landscape by O-H distance and system free energy, the symmetric  
123 H bond is like a double-well energy surface. Hydrogen atoms oscillate between two  
124 stable hydroxyl positions, and the energy barriers between the two positions are  
125 relatively shallow (Tsuchiya et al., 2005). Movement of H may be promoted at high  
126 temperatures, which provide kinetic energy to overcome even higher free energy  
127 barriers out of the defined hydroxyl positions (Zhu et al., 2017). Upon surpassing such  
128 a kinetic barrier, H becomes unconstrained and penetrates the pressure media. The  
129 large-scale movement of H eventually forms a continuous H variation, full-scale

130 FeO<sub>2</sub>-FeO<sub>2</sub>H system at high *P-T*.

131

132 The O-O bond in the pyrite-phase has led an on-going discussion in the fields of high-  
 133 pressure mineralogy and geochemistry. Koemets et al. (2019) suggested that the long  
 134 O-O bonds make Py-FeO<sub>2</sub> closer to a PdF<sub>2</sub>-type structure, which occupies the same  
 135 space group *Pa*<sup>3</sup> but features no anion-anion interactions (Koemets et al., 2019).  
 136 Historically, the same question was raised for Py-SiO<sub>2</sub>, a silica polymorph that is  
 137 stable above ~260 GPa and was discovered 14 years ago (Haines et al., 1996;  
 138 Kuwayama et al., 2005). Py-SiO<sub>2</sub> has O-O bonds greater than 2.4 Å and is arguably a  
 139 so-called 6+2 bonding type with conventional SiO<sub>6</sub> octahedra and weak O-O  
 140 interactions (Kuwayama et al., 2011). On the other hand, Py-FeO<sub>2</sub> has much shorter  
 141 O-O bonds than Py-SiO<sub>2</sub>, so it is reasonable to expect that it does not have  
 142 hypothetical, non-interactive bonding (Lu and Chen, 2018). Meanwhile, X-ray  
 143 absorption experiment results indicated the valence states of Fe at 2+ for both FeO<sub>2</sub>  
 144 and FeO<sub>2</sub>Hx (Boulard et al., 2019; Liu et al., 2019), and confirmed that oxygen atoms  
 145 actively interact.

146

#### 147 **4. The FeO<sub>2</sub>-FeO<sub>2</sub>H system**

148 Py-FeO<sub>2</sub> and Py-Fe<sub>2</sub>H represent the two end members of an iron peroxide-  
 149 oxyhydroxide system (Hu et al., 2016; Nishi et al., 2017; Huang et al., 2018;). While  
 150 the end members are well-defined, whether a complete solid solution is formed by  
 151 varying H is debated. The variation of H is directly relevant to O, H heterogeneities  
 152 that might be the signatures of DLM hydrous phases. Since the lightest element H has  
 153 very low charge density, it is almost invisible on x-ray diffraction. Neutron diffraction,  
 154 a more sensitive probe to H (Sano-Furukawa et al., 2018), is also impractical for  
 155 experiments above megabar pressures (Mao et al., 2018). Therefore, we employed an  
 156 indirect method to evaluate the hydrogen concentration through the unit-cell volume  
 157 of Py-phases. The H content is estimated by comparing the lattice volumes of Py-  
 158 FeO<sub>2</sub>Hx ( $V_x$ ) to the H-free FeO<sub>2</sub> ( $V_0$ ) and calculated volumes of FeO<sub>2</sub> ( $V_{s0}$ ) and H-  
 159 saturated FeO<sub>2</sub>H ( $V_{sI}$ ) using the following equation (Hu et al., 2017):

$$160 \quad x = (V_x - V_0) / (V_{sI} - V_{s0})$$

161 The use of calculated volumes difference  $V_{sI} - V_{s0}$  is a compromise of lack of  
 162 experiment FeOOH EOS. The accuracy of  $x$  will be improved once we verified the  
 163 fully hydrogenated FeOOH EOS (Nishi et al., 2017). This volume method has been

164 generally employed to calculate the H amount in a variety of hydrides and  
165 oxyhydroxides ( Nishi et al., 2017; Pépin et al., 2017; Drozdov et al., 2019; Zhuang et  
166 al., 2019).

167

168 In Fig. 4, we list the *P-V* data of all synthesized Py-phases ( Hu et al., 2017; Liu et al.,  
169 2017; Mao et al., 2017; Nishi et al., 2017; Boulard et al., 2018; Yuan et al., 2018) and  
170 calculated EOS from simulation (Nishi et al., 2017; Hu et al., 2017; Zhang et al., 2017;  
171 Huang et al., 2019; Koemets et al., 2019). The experimental equation of states (EOS)  
172 for Py-FeO<sub>2</sub> and Py-FeO<sub>2</sub>H are also plotted for comparison (Hu et al., 2016; Nishi et  
173 al., 2017). The EOS from first-principles simulation are generally consistent with  
174 experiment, although the local density approximation (LDA) functional  
175 underestimates the volume (*e.g.* -4% at 60 GPa). Generalized gradient approximation  
176 (GGA) performs quite differently for FeO<sub>2</sub> and FeO<sub>2</sub>H. It overestimates FeO<sub>2</sub>H  
177 volumes while underestimates FeO<sub>2</sub> volumes. The opposite functional correlation may  
178 stem from their completely different electronic structures due to the O-O molecular  
179 orbitals (Shorikov et al., 2018). Calculated EOS by setting a very high kinetic cutoff  
180 energy (*e.g.* 1000 eV by Huang et al., 2018) or employing the density mean-field  
181 theory (DFT+DMFT, by Koemet et al., 2019) improve accuracy and almost reproduce  
182 the experimental EOS.

183

184 The scattering of experimental volume data is more interesting. Rather than  
185 disagreeing, the experimental data points seem consistent with each other with a  
186 reasonable amount of variation. However, statistics indicate that pressure may play an  
187 important role in the hydrogenation of Py-FeO<sub>2</sub>. At higher pressures (*e.g.*, > 100 GPa),  
188 the Py-phase prefers a higher H content and approaches H saturation at the pressures  
189 found at the bottom of Earth's core-mantle boundary. On the other hand, those low *x*  
190 volumes are likely to scatter between 70 GPa and 90 GPa. The collection of data  
191 indicate pressure may increasingly suppress the hydrogen differentiation in the Py-  
192 FeO<sub>2</sub>H<sub>x</sub>. Once synthesized at those higher pressures, the volume of Py-FeO<sub>2</sub>H<sub>x</sub> is  
193 close to the EOS of FeO<sub>2</sub>H end member presented by Nishi (Nishi et al., 2017).  
194 However, their lattice volumes are still well below the FeO<sub>2</sub>+0.5H<sub>2</sub> cap line. Thus, it  
195 is possible that the EOS of FeO<sub>2</sub>H in Fig. 4 represents a preferred Py-FeO<sub>2</sub>H<sub>x</sub>  
196 composition between FeO<sub>2</sub> and FeO<sub>2</sub>H; for example, the FeO<sub>2</sub>H<sub>0.75</sub> predicted by first-  
197 principles simulation (He et al., 2018). Since H in the Py-type structure is highly

mobile, it is considerably challenging to quantify H in experiment. Either identifying a fully hydrogenated Py- $\text{FeO}_2\text{H}$  or predicting the energetically stable  $\text{FeO}_2\text{H}_x$  compositions under different pressures still await future investigation.

201

202 Compared to the  $P$ - $x$  relation, the  $T$  dependence on the  $x$  is more technically  
 203 challenging. In addition to pressure (the primary parameter for high-pressure  
 204 experiments), laser heating is generally controlled by two factors: heating temperature  
 205  $T$  and heating duration. Therefore, it is necessary to fix thermodynamic parameters  
 206 like pressure and heating duration for data points representing the  $T$ - $x$  relation.  
 207 However, due to thermal equilibrium, it is impractical to repeat individual  
 208 experiments at the exact same pressure. The laser power cannot be precisely  
 209 controlled or stabilized manually during the heating. In Fig. 5, we compromised to  
 210 select volumes from a pressure range (80–90 GPa) and similar heating time (generally  
 211 around 5 min). We chose the narrow pressure range such that the variance of  $x$  is in a  
 212 wider range. The uncertainty of  $x$  considers the peak indexing error, the refinement  
 213 error and the error in comparing the EOS of  $\text{FeO}_2$  and  $\text{FeO}_2\text{H}$ . The combined  
 214 uncertainty is up to 0.06. The linear regression fit for  $T$ - $x$  shows a negative slope with  
 215 the goodness of fit  $R^2=0.78$ . The fitting result indicates that the linear relation may  
 216 represent the majority of experimental data. The higher the temperature, the more H  
 217 loss from the pyrite-type lattice. It is worth noting that such a linear relation only  
 218 applies to limited  $T$  (e.g., < 2400 K). At higher  $T$ s and the same heating duration,  
 219 further release of H was not observed in the literature.

220

221 In short, both  $P$  and heating  $T$  are important thermodynamic variables in controlling  
 222 the lattice volumes of Py- $\text{FeO}_2\text{H}_x$ . The variation of H content  $x$  becomes constrained  
 223 at higher pressures and may approximate to the fully hydrogenated Py- $\text{FeO}_2\text{H}$  (Nishi  
 224 et al., 2017) or a stable H-enriched Py- $\text{FeO}_2\text{H}_x$  composition with a certain amount of  
 225 H in the lattice. However, the direct determination of the  $x$  values in  $\text{FeO}_2\text{H}_x$  requires  
 226 the development of specialized probes for H under high pressures.

227

## 228 **5. Separation of high- $x$ and low- $x$ phases in $\text{FeO}_2\text{H}_x$**

229 Although the perturbation of volumes along the equation of states provides evidence  
 230 of H variation in the  $\text{FeO}_2$ - $\text{FeO}_2\text{H}$  system, characterizing a partial hydrogenation  
 231 process is a key to define the H release in  $\text{FeO}_2\text{H}_x$ . The computational simulation

predicted that H is quantumized in the FeO<sub>2</sub>-FeO<sub>2</sub>H system(He et al., 2018). The tie-line connecting FeO<sub>2</sub> and FeO<sub>2</sub>H passes a few metastable structures with  $x=0, 0.25, 0.5, 0.75$ , and  $1$ . The computation results also indicate that by releasing a quarter of the total H, Py-FeO<sub>2</sub>H<sub>0.75</sub> is the ground state in the FeO<sub>2</sub>-FeO<sub>2</sub>H system. While the stepwise release of H is not surprising for hydrides and hydrogen-storage materials(Lin and Mao, 2014), direct observation of those metastable structures usually involve tracking chemical kinetics, which is achieved by controlling the pressurization rates, e.g., dynamic compression(Chen et al., 2014; Lee et al., 2007). However, this is challenging for DAC experiments, which are generally designed for static compression without controlling the compression rate. Here, through dynamic decompression, the following experiments eventually separated the sample into coexisting high- $x$  and low- $x$  phases in FeO<sub>2</sub>H $x$  at 53 GPa and room temperature.

Dynamic compression or decompression was introduced to the DAC in 2007 by Evans et al. (2007), who successfully used a piezoelectric actuator to control the DAC pressurization rate. With the help of controlled piezoelectric actuators, their design (called dDAC) enables pressure loading rates of 500 GPa/s. We borrowed the same idea to quench one Py-FeO<sub>2</sub>H $x$  sample from 121 GPa to 53 GPa within a few seconds. Upon removing more than half of its pressure, the sample separated into two Py-phases with more than 10.7% volume difference (Fig. 6). the low-high spin transition in FeO<sub>2</sub>H $x$  occurs between 49 GPa and 62 GPa, which may contribute a portion of the volume difference. However, the observed difference is at least four times greater than the one merely by spin transition (Jang et al., 2019; Liu et al., 2019). We also carefully checked the pressure gradient by XRD mapping over the sample chamber (Fig. 7). The two Py-phases are geometrically separated but have an overlapped region at the center of the sample chamber. Here, the Au pressure calibrant or the ice pressure medium gives  $\pm 4$  GPa pressure at most. Therefore, the big volume gap has to be filled by both a spin transition and the varying H content  $x$ . The low  $x$  (L $x$ ) phase has a lattice parameter of 4.5598(6) Å, and high  $x$  (H $x$ ) has a lattice parameter of 4.7167(6) Å. Since the spin transition contribution to the volume change is not clearly defined, we did not estimate the exact  $x$  in each phase. However, a 10.7% volume difference may represent the amount between end members of FeO<sub>2</sub> and FeO<sub>2</sub>H at higher pressures (Hu et al., 2017). If we assume the L $x$  and H $x$  Py-phases are in the same spin state, they are close to the two end members. Although the dynamic

266 decompression process was not fully controlled in the current setup, it will be helpful  
267 to clearly identify the effect of varying hydrogen content without introducing the spin-  
268 transition effects. That is, as soon as technically allowed, experiments performed  
269 within the same spin configuration may provide more constraints to the phase  
270 separation behaviors of the Py-phase.

271

## 272 **6. Summary**

273 Variation of H in the pyrite-type FeO<sub>2</sub>-FeO<sub>2</sub>H system profoundly influences the H  
274 cycling of solid Earth. While the H budget at Earth's DLM remains unknown, the  
275 evolution of hydrous phases from the shallower mantle to deeper interiors has become  
276 even more intriguing for mineralogists. Fundamental elements like O and H tend to  
277 exhibit exotic chemical properties upon reaching critical pressures (e.g., 70–80 GPa),  
278 leading to the formation of peroxide phases like the Py-phase. The compositional  
279 change may form chemical discontinuity around 1800 km in the lower mantle (Fig. 8),  
280 above which the thermal stability of hydrous phases are clearly defined by the  
281 dehydration conditions (Tsuchiya, 2013; Tsuchiya and Umemoto, 2019). Such criteria  
282 make most Al-free DHPs terminate at a depth of ~1500 km in the middle of the lower  
283 mantle (Tsuchiya and Umemoto, 2019). It is also not surprising that when the same  
284 criteria are applied to the FeO<sub>2</sub>-FeO<sub>2</sub>H system, theoretical calculations predict that the  
285 H-bearing Py-phase is thermodynamically unstable (Nishi et al., 2017). The  
286 experimental controversy lies in the fact that below the chemical discontinuity line, H  
287 releases from Py-FeO<sub>2</sub>H, and the *T* in the DLM is far beyond the melting temperature  
288 of solid hydrogen (Howie et al., 2015). The tremendous entropy added by the solid-  
289 liquid phase transition may create significant difficulties for theoretical energy  
290 calculations. Consequently, calculations may underestimate the free energy of H to  
291 reverse the phase stability of Py-FeO<sub>2</sub>Hx. On the other hand, the high mobility of  
292 liquid H is also consistent with a couple of recent studies on H-bearing phases and  
293 deep hydrogen cycling. As a light volatile element, H may substitute the cation of  
294 mantle silicates (Townsend et al., 2016), bond with volatiles like C to form  
295 hydrocarbon (Stagno et al., 2013) or penetrate the outer core (Ohira et al., 2014). The  
296 incorporation of H lowers the density of silicate which may ascend to the shallower  
297 mantle. This deep mantle chemistry provides a mechanism to recycle a fraction of  
298 hydrogen through the formation of low-density silicates and hydrocarbons.

299

300 The dehydrogenation process is also vital for seismological observations. For example,  
 301 the dehydrogenation of amphibole can explain the seismic discontinuity at the mantle  
 302 transition zone (Hu et al., 2018). Dehydrogenation in the DLM, similarly, creates  
 303 oxygen-rich patches like Py-FeO<sub>2</sub> and Py-FeO<sub>2</sub>Hx that also account for seismological  
 304 heterogeneities (Liu et al., 2017; Mao et al., 2017)(Fig. 8). While many mechanisms  
 305 have been proposed for those observations Mao et al., 2006; Brown et al., 2015; Liu  
 306 et al., 2016), the Py-phase appears to provide a more robust solution to the  
 307 seismological anomalies observed in some ultra-low velocity zones (Deng et al., 2019;  
 308 Liu et al., 2017). In conclusion, the FeO<sub>2</sub>-FeO<sub>2</sub>H system creates very different  
 309 mineralogy located at the DLM. The properties of H in this system are still under  
 310 substantial research, but these results shed new light on the evolution and dynamics of  
 311 our planet.

312

### 313 **Acknowledge**

314 The authors thank Y. Meng, D. Zhang, V. B. Prakapenka, and E. Greenberg for  
 315 assistance with conducting synchrotron X-ray diffraction experiments. The authors  
 316 also acknowledge F. O'Toole for proofreading the manuscript. The work is partially  
 317 supported by NSAF (Grant Nos. U1530402 and U1930401) and National Natural  
 318 Science Foundation of China (NSFC, Grant No. 17N1051-0213). The authors  
 319 conducted x-ray diffraction experiments at the GeoSoilEnviroCARS (GSECARS) and  
 320 High-Pressure Collaborative Access Team (HPCAT) sectors of Advanced Photon  
 321 Source. GSECARS is supported by the National Science Foundation - Earth Sciences  
 322 (EAR-1128799) and the Department of Energy - Geosciences (DE-FG02-  
 323 94ER14466). HPCAT operations are supported by DOE-NNSA's Office of  
 324 Experimental Sciences. APS is supported by DOE-BES, under contract no. DE-  
 325 AC02-06CH11357.

326

### 327 **References**

- 328 Akahama, Y., Kawamura, H., Häusermann, D., Hanfland, M., Shimomura, O., 1995. New high-  
 329 pressure structural transition of oxygen at 96 GPa associated with metallization in a molecular solid.  
 330 Phys. Rev. Lett. 74, 4690-4693.
- 331 Boulard, E., Guyot, F., Menguy, N., Corgne, A., Auzende, A.-L., Perrillat, J.-P., Fiquet, G., 2018. CO<sub>2</sub>-  
 332 induced destabilization of pyrite-structured FeO<sub>2</sub>Hx in the lower mantle. Natl. Sci. Rev. 5, 870-877.
- 333 Boulard, E., Harmand, M., Guyot, F., Lelong, G., Morard, G., Cabaret, D., Boccato, S., Rosa, A.D.,  
 334 Briggs, R., Pascarelli, S., Fiquet, G., 2019. Ferrous iron under oxygen-rich conditions in the deep  
 335 mantle. Geophys. Res. Lett. 46, 1348-1356.

- 336 Brown, S.P., Thorne, M.S., Miyagi, L., Rost, S., 2015. A compositional origin to ultralow-velocity  
 337 zones. *Geophys. Res. Lett.* 42, 1039-1045.
- 338 Bykova, E., Dubrovinsky, L., Dubrovinskaia, N., Bykov, M., McCammon, C., Ovsyannikov, S.V.,  
 339 Liermann, H.P., Kupenko, I., Chumakov, A.I., Ruffer, R., Hanfland, M., Prakapenka, V., 2016.  
 340 Structural complexity of simple  $\text{Fe}_2\text{O}_3$  at high pressures and temperatures. *Nat. Commun.* 7, 10661.
- 341 Chen, J.-Y., Yoo, C.-S., Evans, W.J., Liermann, H.-P., Cynn, H., Kim, M., Jenei, Z., 2014.  
 342 Solidification and fcc to metastable hcp phase transition in krypton under variable compression rates.  
 343 *Phys. Rev. B* 90, 144104.
- 344 Deng, J., Karki, B.B., Ghosh, D.B., Lee, K.K.M., 2019. First-principles study of  $\text{FeO}_2\text{Hx}$  solid and  
 345 melt system at high pressures: Implications for ultralow-velocity zones. *J. Geophys. Res.: Solid Earth*  
 346 124, 4566-4575.
- 347 Drozdov, A.P., Kong, P.P., Minkov, V.S., Besedin, S.P., Kuzovnikov, M.A., Mozaffari, S., Balicas, L.,  
 348 Balakirev, F.F., Graf, D.E., Prakapenka, V.B., Greenberg, E., Knyazev, D.A., Tkacz, M., Eremets, M.I.,  
 349 2019. Superconductivity at 250 K in lanthanum hydride under high pressures. *Nature* 569, 528-531.
- 350 Evans, W.J., Yoo, C.-S., Lee, G.W., Cynn, H., Lipp, M.J., Visbeck, K., 2007. Dynamic diamond anvil  
 351 cell (dDAC): A novel device for studying the dynamic-pressure properties of materials. *Rev. Sci.*  
 352 *Instrum.* 78, 073904.
- 353 Fei, Y., Ricolleau, A., Frank, M., Mibe, K., Shen, G., Prakapenka, V., 2007. Toward an internally  
 354 consistent pressure scale. *Proc. Natl. Acad. Sci. U. S. A.* 104, 9182-9186.
- 355 Haines, J., Léger, J.M., Schulte, O., 1996. Pa3 modified fluorite-type structures in metal dioxides at  
 356 high pressure. *Science* 271, 629-631.
- 357 He, Y., Kim, D., Pickard, C.J., Needs, R.J., Hu, Q., Mao, H.-k., 2018. Superionic hydrogen in Earth's  
 358 deep interior. *arXiv*, 1810.08766.
- 359 Heinz, D.L., Jeanloz, R., 1984. The equation of state of the gold calibration standard. *J. Appl. Phys.* 55,  
 360 885-893.
- 361 Hoffman, C., Ropp, R., Mooney, R., 1959. Preparation, properties and structure of cadmium peroxide.  
 362 *J. Am. Chem. Soc.* 81, 3830-3834.
- 363 Howie, R.T., Dalladay-Simpson, P., Gregoryanz, E., 2015. Raman spectroscopy of hot hydrogen above  
 364 200 GPa. *Nat. Mater.* 14, 495-499.
- 365 Hu, H., Dai, L., Li, H., Sun, W., Li, B., 2018. Effect of dehydrogenation on the electrical conductivity  
 366 of Fe-bearing amphibole: Implications for high conductivity anomalies in subduction zones and  
 367 continental crust. *Earth Planet. Sci. Lett.* 498, 27-37.
- 368 Hu, Q., Kim, D.Y., Liu, J., Meng, Y., Yang, L., Zhang, D., Mao, W.L., Mao, H.-k., 2017.  
 369 Dehydrogenation of goethite in Earth's deep lower mantle. *Proc. Nat. Acad. Sci. U.S.A.* 114, 1498-  
 370 1501.
- 371 Hu, Q., Kim, D.Y., Yang, W., Yang, L., Meng, Y., Zhang, L., Mao, H.-K., 2016.  $\text{FeO}_2$  and  $\text{FeOOH}$   
 372 under deep lower-mantle conditions and Earth's oxygen-hydrogen cycles. *Nature* 534, 241.
- 373 Huang, S., Wu, X., Qin, S., 2018. Ultrahigh-pressure phase transitions in  $\text{FeS}_2$  and  $\text{FeO}_2$ : Implications  
 374 for super-Earths' deep interior. *J. Geophys. Res.: Solid Earth* 123, 277-284.
- 375 Huang, S., Qin, S., Wu, X., 2019. Elasticity and anisotropy of the pyrite-type  $\text{FeO}_2\text{H}$ - $\text{FeO}_2$  system in  
 376 Earth's lowermost mantle. *J. Earth. Sci.* 30, 1293-1301
- 377 Ito, E., Yamazaki, D., Yoshino, T., Fukui, H., Zhai, S., Shatzkiy, A., Katsura, T., Tange, Y., Funakoshi,

- 378 K.-i., 2010. Pressure generation and investigation of the post-perovskite transformation in MgGeO<sub>3</sub> by  
379 squeezing the Kawai-cell equipped with sintered diamond anvils. *Earth Planet. Sci. Lett.* 293, 84-89.
- 380 Jang, B.G., Liu, J., Hu, Q., Haule, K., Mao, H.-K., Mao, W.L., Kim, D.Y., Shim, J.H., 2019. Electronic  
381 spin transition in FeO<sub>2</sub>: Evidence for Fe(II) with peroxide O<sub>2</sub><sup>2-</sup>. *Phys. Rev. B* 100, 014418.
- 382 Jephcoat, A.P., Mao, H.-K., Bell, P.M., 1987. *Hydrothermal Experiment Techniques*. Wiley-  
383 interscience.
- 384 Koemets, E., Bykov, M., Bykova, E., Chariton, S., Aprilis, G., Clément, S., Rouquette, J., Haines, J.,  
385 Cerantola, V., Glazyrin, K., Abakumov, A., Ismailova, L., McCammon, C., Prakapenka, V.B., Hanfland,  
386 M., Liermann, H.-P., Leonov, I., Ponomareva, A.V., Abrikosov, I.A., Dubrovinskaia, N., Dubrovinsky,  
387 L., 2019. Variation of oxygen oxidation state at the base of Earth's lower mantle. *arXiv*, 1905.05497.
- 388 Kuwayama, Y., Hirose, K., Sata, N., Ohishi, Y., 2005. The pyrite-type high-pressure form of silica.  
389 *Science* 309, 923-925.
- 390 Kuwayama, Y., Hirose, K., Sata, N., Ohishi, Y., 2011. Pressure-induced structural evolution of pyrite-  
391 type SiO<sub>2</sub>. *Phys. Chem. Miner.* 38, 591-597.
- 392 Lavina, B., Dera, P., Kim, E., Meng, Y., Downs, R.T., Weck, P.F., Sutton, S.R., Zhao, Y., 2011.  
393 Discovery of the recoverable high-pressure iron oxide Fe<sub>4</sub>O<sub>5</sub>. *Proc. Natl. Acad. Sci. U.S.A.* 108,  
394 17281-17285.
- 395 Lavina, B., Meng, Y., 2015. Unraveling the complexity of iron oxides at high pressure and temperature:  
396 Synthesis of Fe<sub>5</sub>O<sub>6</sub>. *Sci. Adv.* 1, e1400260.
- 397 Lee, G.W., Evans, W.J., Yoo, C.-S., 2007. Dynamic pressure-induced dendritic and shock crystal  
398 growth of ice VI. *Proc. Natl. Acad. Sci. U.S.A.* 104, 9178-9181.
- 399 Lin, Y., Hu, Q., Meng, Y., Walter, M., Mao, H.-K., 2020. Evidence for the stability of ultrahydrous  
400 stishovite in Earth's lower mantle. *Proc. Nat. Acad. Sci. U.S.A.* 117, 184-189.
- 401 Lin, Y., Mao, W.L., 2014. High-pressure storage of hydrogen fuel: ammonia borane and its related  
402 compounds. *Chin. Sci. Bull.* 59, 5235-5240.
- 403 Liu, J., Hu, Q., Bi, W., Yang, L., Xiao, Y., Chow, P., Meng, Y., Prakapenka, V.B., Mao, H.K., Mao,  
404 W.L., 2019. Altered chemistry of oxygen and iron under deep Earth conditions. *Nat. Commun.* 10, 153.
- 405 Liu, J., Hu, Q., Kim, D.Y., Wu, Z., Wang, W., Xiao, Y., Chow, P., Meng, Y., Prakapenka, V.B., Mao, H.-  
406 K., 2017. Hydrogen-bearing iron peroxide and the origin of ultralow-velocity zones. *Nature* 551, 494.
- 407 Liu, J., Li, J., Hrubík, R., Smith, J.S., 2016. Origins of ultra-low velocity zones through slab-derived  
408 metallic melt. *Proc. Nat. Acad. Sci. U.S.A.* 113, 5547-5551.
- 409 Lu, C., Chen, C., 2018. High-pressure evolution of crystal bonding structures and properties of  
410 FeOOH. *J. Phys. Chem. Lett.* 9, 2181-2185.
- 411 Mao, H.-K., Chen, X.-J., Ding, Y., Li, B., Wang, L., 2018. Solids, liquids, and gases under high  
412 pressure. *Rev. Mod. Phys.* 90, 015007.
- 413 Mao, H.-K., Hu, Q., Yang, L., Liu, J., Kim, D.Y., Meng, Y., Zhang, L., Prakapenka, V.B., Yang, W.,  
414 Mao, W.L., 2017. When water meets iron at Earth's core-mantle boundary. *Natl. Sci. Rev.* 4, 870-878.
- 415 Mao, H.K., Xu, J., Bell, P.M., 1986. Calibration of the ruby pressure gauge to 800 kbar under quasi-  
416 hydrostatic conditions. *J. Geophys. Res.: Solid Earth* 91, 4673-4676.
- 417 Mao, W.L., Mao, H.-K., Sturhahn, W., Zhao, J., Prakapenka, V.B., Meng, Y., Shu, J., Fei, Y., Hemley,  
418 R.J., 2006. Iron-rich post-perovskite and the origin of ultralow-velocity zones. *Science* 312, 564-565.

- 419 Meng, Y., Hrubiak, R., Rod, E., Boehler, R., Shen, G., 2015. New developments in laser-heated  
 420 diamond anvil cell with in-situ x-ray diffraction at High Pressure Collaborative Access Team. Rev. Sci.  
 421 Instrum. 86, 072201.
- 422 Merlini, M., Hanfland, M., Salamat, A., Petitgirard, S., Müller, H., 2015. The crystal structures of  
 423  $Mg_2Fe_2C_4O_{13}$ , with tetrahedrally coordinated carbon, and  $Fe_{13}O_{19}$ , synthesized at deep mantle  
 424 conditions. Am. Miner. 100, 2001-2004.
- 425 Nishi, M., Kuwayama, Y., Tsuchiya, J., Tsuchiya, T., 2017. The pyrite-type high-pressure form of  
 426 FeOOH. Nature 547, 205.
- 427 Nishi, M., Tsuchiya, J., Arimoto, T., Kakizawa, S., Kunimoto, T., Tange, Y., Higo, Y., Irifune, T., 2018.  
 428 Thermal equation of state of  $MgSiO_4H_2$  phase H determined by *in situ* X-ray diffraction and a  
 429 multianvil apparatus. Phys. Chem. Miner. 45, 995-1001.
- 430 Nishi, M., Tsuchiya, J., Kuwayama, Y., Arimoto, T., Tange, Y., Higo, Y., Hatakeyama, T., Irifune, T.,  
 431 2019. Solid solution and compression behavior of hydroxides in the lower mantle. J. Geophys. Res.:  
 432 Solid Earth 0.
- 433 Ohira, I., Ohtani, E., Sakai, T., Miyahara, M., Hirao, N., Ohishi, Y., Nishijima, M., 2014. Stability of a  
 434 hydrous  $\delta$ -phase, AlOOH– $MgSiO_2(OH)_2$ , and a mechanism for water transport into the base of lower  
 435 mantle. Earth Planet. Sci. Lett. 401, 12-17.
- 436 Ohtani, E., 2019. The role of water in Earth's mantle. Natl. Sci. Rev.
- 437 Pépin, C.M., Geneste, G., Dewaele, A., Mezouar, M., Loubeire, P., 2017. Synthesis of  $FeH_5$ : A layered  
 438 structure with atomic hydrogen slabs. Science 357, 382.
- 439 Sano-Furukawa, A., Hattori, T., Komatsu, K., Kagi, H., Nagai, T., Molaison, J.J., dos Santos, A.M.,  
 440 Tulk, C.A., 2018. Direct observation of symmetrization of hydrogen bond in  $\delta$ -AlOOH under mantle  
 441 conditions using neutron diffraction. Sci. Rep. 8, 15520.
- 442 Santamaría-Pérez, D., Mukherjee, G.D., Schwager, B., Boehler, R., 2010. High-pressure melting curve  
 443 of helium and neon: Deviations from corresponding states theory. Phys. Rev. B 81, 214101.
- 444 Shorikov, A.O., Poteryaev, A.I., Anisimov, V.I., Streltsov, S.V., 2018. Hydrogenation-driven formation  
 445 of local magnetic moments in  $FeO_2Hx$ . Phys. Rev. B 98, 165145.
- 446 Sinmyo, R., Bykova, E., Ovsyannikov, S.V., McCammon, C., Kupenko, I., Ismailova, L., Dubrovinsky,  
 447 L., 2016. Discovery of  $Fe_7O_9$ : a new iron oxide with a complex monoclinic structure. Sci. Rep. 6,  
 448 32852.
- 449 Stagno, V., Ojwang, D.O., McCammon, C.A., Frost, D.J., 2013. The oxidation state of the mantle and  
 450 the extraction of carbon from Earth's interior. Nature 493, 84.
- 451 Townsend, J.P., Tsuchiya, J., Bina, C.R., Jacobsen, S.D., 2016. Water partitioning between bridgmanite  
 452 and postperovskite in the lowermost mantle. Earth and Planet. Sci. Lett. 454, 20-27.
- 453 Tsuchiya, J., 2013. First principles prediction of a new high-pressure phase of dense hydrous  
 454 magnesium silicates in the lower mantle. Geophys. Res. Lett. 40, 4570-4573.
- 455 Tsuchiya, J., Tsuchiya, T., Tsuneyuki, S., 2005. First-principles study of hydrogen bond symmetrization  
 456 of phase D under high pressure. Am. Miner. 90, 44–49.
- 457 Tsuchiya, J., Tsuchiya, T., Tsuneyuki, S., Yamanaka, T., 2002. First principles calculation of a high-  
 458 pressure hydrous phase,  $\delta$ -AlOOH. Geophys. Res. Lett. 29, 1-4.
- 459 Tsuchiya, J., Umemoto, K., 2019. First-principles determination of the dissociation phase boundary of  
 460 phase H  $MgSiO_4H_2$ . Geophys. Res. Lett. 46, 7333-7336.

- 461 Weerasinghe, G.L., Pickard, C.J., Needs, R.J., 2015. Computational searches for iron oxides at high  
462 pressures. *J. Phys.: Condens. Matter* 27, 455501.
- 463 Xu, C., Nishi, M., Inoue, T., 2019. Solubility behavior of  $\delta$ -AlOOH and  $\varepsilon$ -FeOOH at high pressures.  
464 *Am. Miner.* 104, 1416-1420.
- 465 Yuan, L., Ohtani, E., Ikuta, D., Kamada, S., Tsuchiya, J., Naohisa, H., Ohishi, Y., Suzuki, A., 2018.  
466 Chemical reactions between Fe and H<sub>2</sub>O up to megabar pressures and implications for water storage in  
467 the Earth's mantle and core. *Geophys. Res. Lett.* 45, 1330-1338.
- 468 Zhang, J., Lv, J., Li, H., Feng, X., Lu, C., Redfern, S.A.T., Liu, H., Chen, C., Ma, Y., 2018a. Rare  
469 helium-bearing compound FeO<sub>2</sub>He stabilized at deep-Earth conditions. *Phys. Rev. Lett.* 121, 255703.
- 470 Zhang, L., Yuan, H., Meng, Y., Mao, H.-k., 2018b. Discovery of a hexagonal ultradense hydrous phase  
471 in (Fe,Al)OOH. *Proc. Nat. Acad. Sci. U.S.A.* 115, 2908-2911.
- 472 Zhang, X.-L., Niu, Z.-W., Tang, M., Zhao, J.-Z., Cai, L.-C., 2017. First-principles thermoelasticity and  
473 stability of pyrite-type FeO<sub>2</sub> under high pressure and temperature. *J. Alloy. Phys.* 719, 42-46.
- 474 Zhu, S.-c., Hu, Q., Mao, W.L., Mao, H.-k., Sheng, H., 2017. Hydrogen-bond symmetrization  
475 breakdown and dehydrogenation mechanism of FeO<sub>2</sub>H at high pressure. *J. Am. Chem. Soc.* 139,  
476 12129-12132.
- 477 Zhu, S.-c., Liu, J., Hu, Q., Mao, W.L., Meng, Y., Zhang, D., Mao, H.-k., Zhu, Q., 2019. Structure-  
478 controlled oxygen concentration in Fe<sub>2</sub>O<sub>3</sub> and FeO<sub>2</sub>. *Inorg. Chem.* 58, 5476-5482.
- 479 Zhuang, Y., Cui, Z., Zhang, D., Liu, J., Tao, R., Hu, Q., 2019. Experimental evidence for partially  
480 dehydrogenated  $\varepsilon$ -FeOOH. *Crystals* 9, 356.
- 481
- 482

483 **Figure caption**

484

485 Figure 1. A sketch setup of *in situ* high  $P$ - $T$  X-ray diffraction experiment coupled with  
486 double-sided laser-heating for a sample in a diamond anvil cell.

487

488 Figure 2. The pyrite-type structure. The structure represents a chemical formula  
489  $\text{FeO}_2\text{H}_{0.5}$ , where the half-black balls indicate the H has a partial occupancy of 0.5.

490

491 Figure. 3. Representative powder refinement for  $\text{FeO}_2\text{H}_x$  at 118 GPa and  
492 quench form 1800 K. Details of structural information are summarized in Table 1. X-  
493 ray wavelength is 0.4066 Å.

494

495 Figure 4. Volumes of Py- $\text{FeO}_2$  and Py- $\text{FeO}_2\text{H}_x$  under pressure. The upper panel  
496 contains experimental data. Open circles are data points imported from references.  
497 The solid grey line sketches statistic minimum volumes of the Py-phases. The release  
498 of H is suppressed above megabar pressures. The lower panel contains results from  
499 first-principles simulation, comparing with EOS curves from experiment.

500

501 Figure 5. Volume vs. heating temperatures for data points with similar heating  
502 durations (~5 min). Data points are from Hu et al. (2017). The linear regression model  
503 indicates that the H content  $x$  from a majority of Py- $\text{FeO}_2\text{H}_x$  experimental runs  
504 follows a linear relation with  $T$ . For the uncertainty of pressure, we estimate  $\pm 0.5$  GPa  
505 from indexing and up to  $\pm 2.0$  GPa from pressure calibrators. The prorogated total  
506 uncertainty is  $\pm 2.1$  GPa.

507

508 Figure 6. Rietveld refinement for the coexistence of high-H and low-H Py-phases.  
509 The diffraction spectra on the left panel were taken at 53 GPa. The right panel is the  
510 2-D diffraction pattern collected by the detector. The refinement factors are  $R_1=0.038$ ,  
511  $wR_2=0.071$ . Abbreviations: Hx-Py, high  $x$  Py-phase; Lx-Py, low  $x$  Py-phase.

512

513 Figure 7. Separation of high- $x$  and low- $x$  phases. The sample area ( $\sim 35 \mu\text{m} \times 35 \mu\text{m}$ ) is  
514 divided into a  $7 \times 7$  matrix. The diffraction map is constructed by tracing the intensity  
515 of signature (111) diffraction peak on each matrix point.

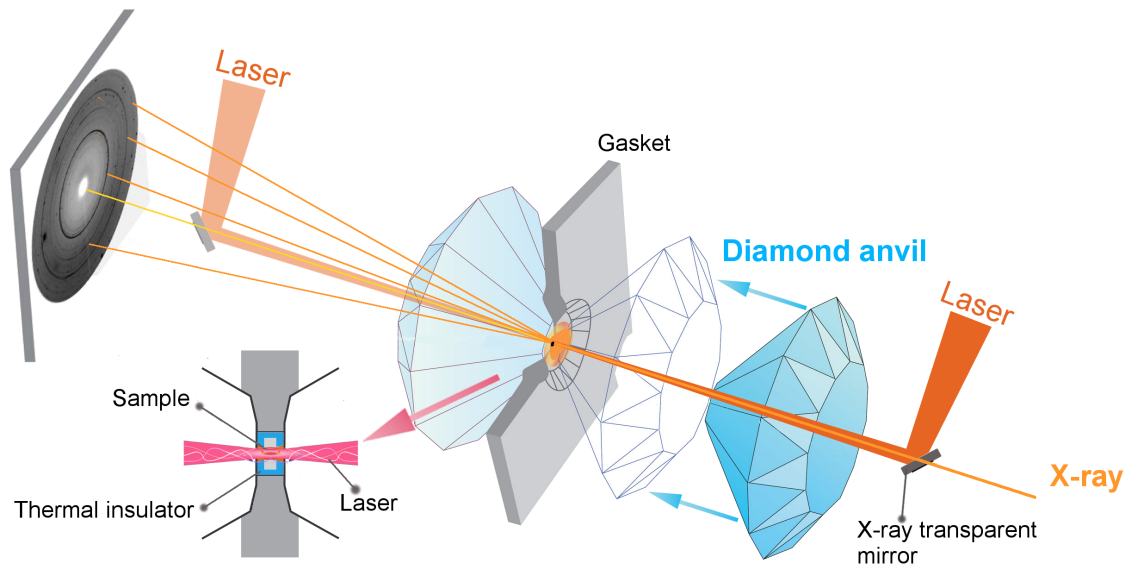
516

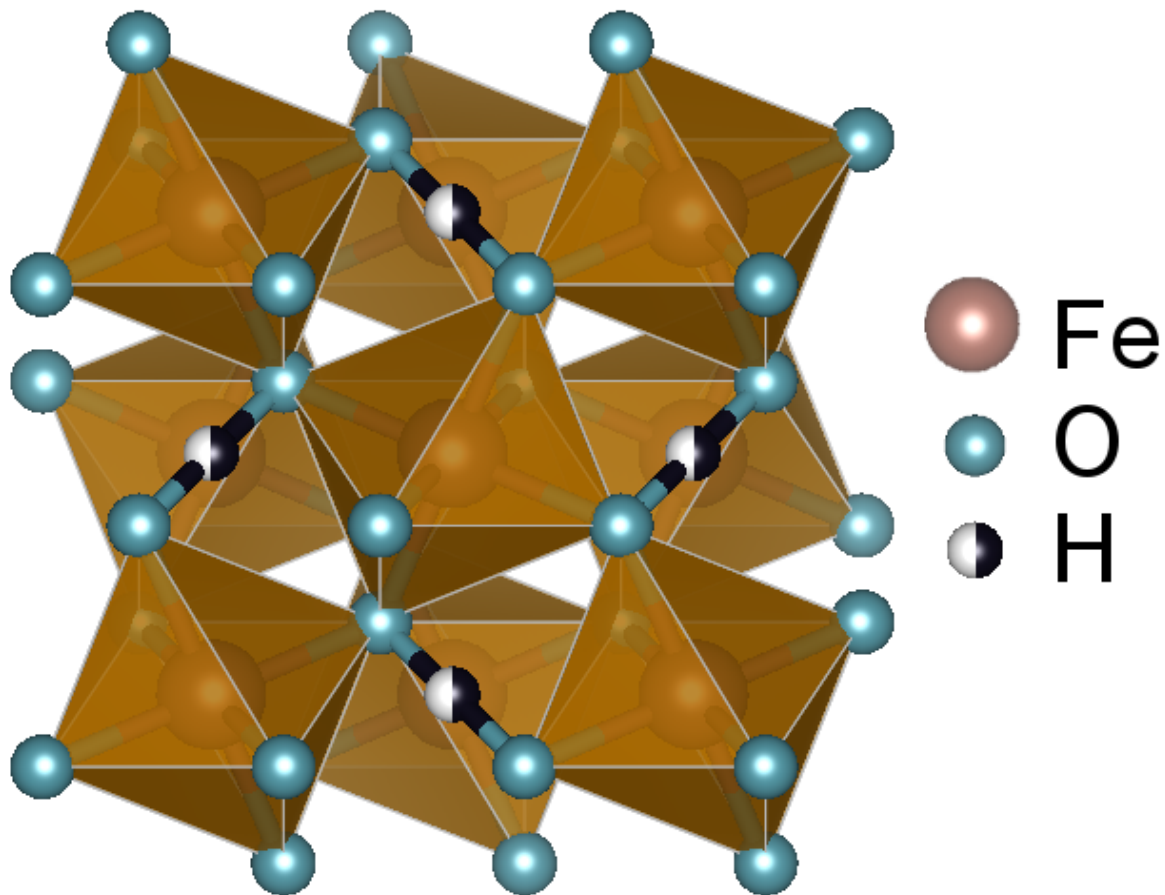
517 Figure 8. Schematic figure for the transportation of H in deep Earth.

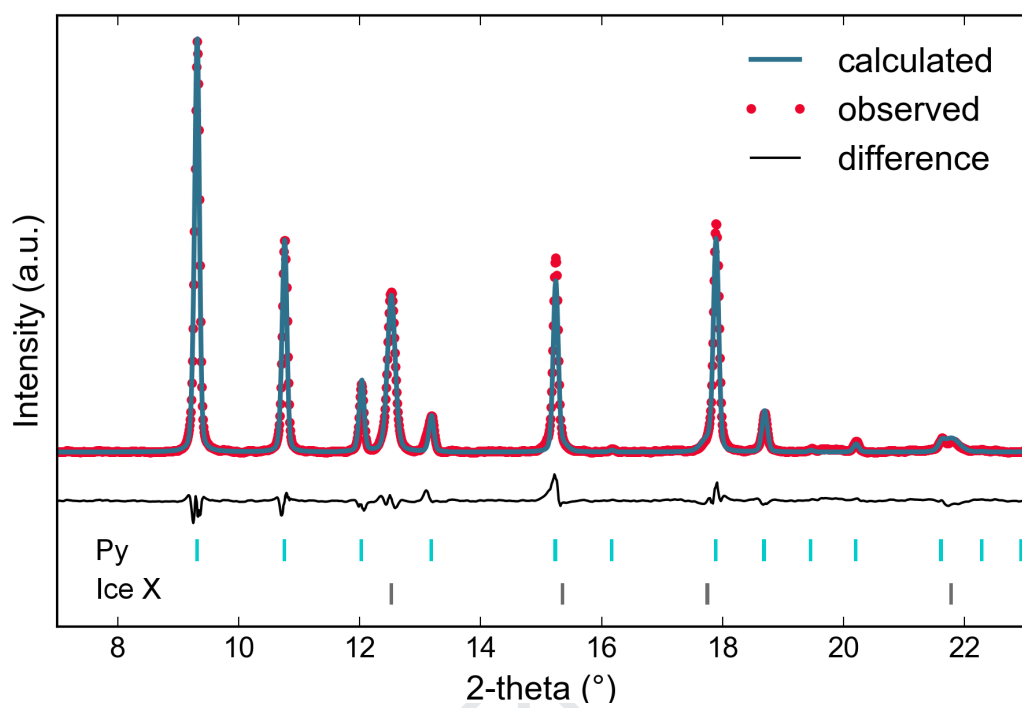
518

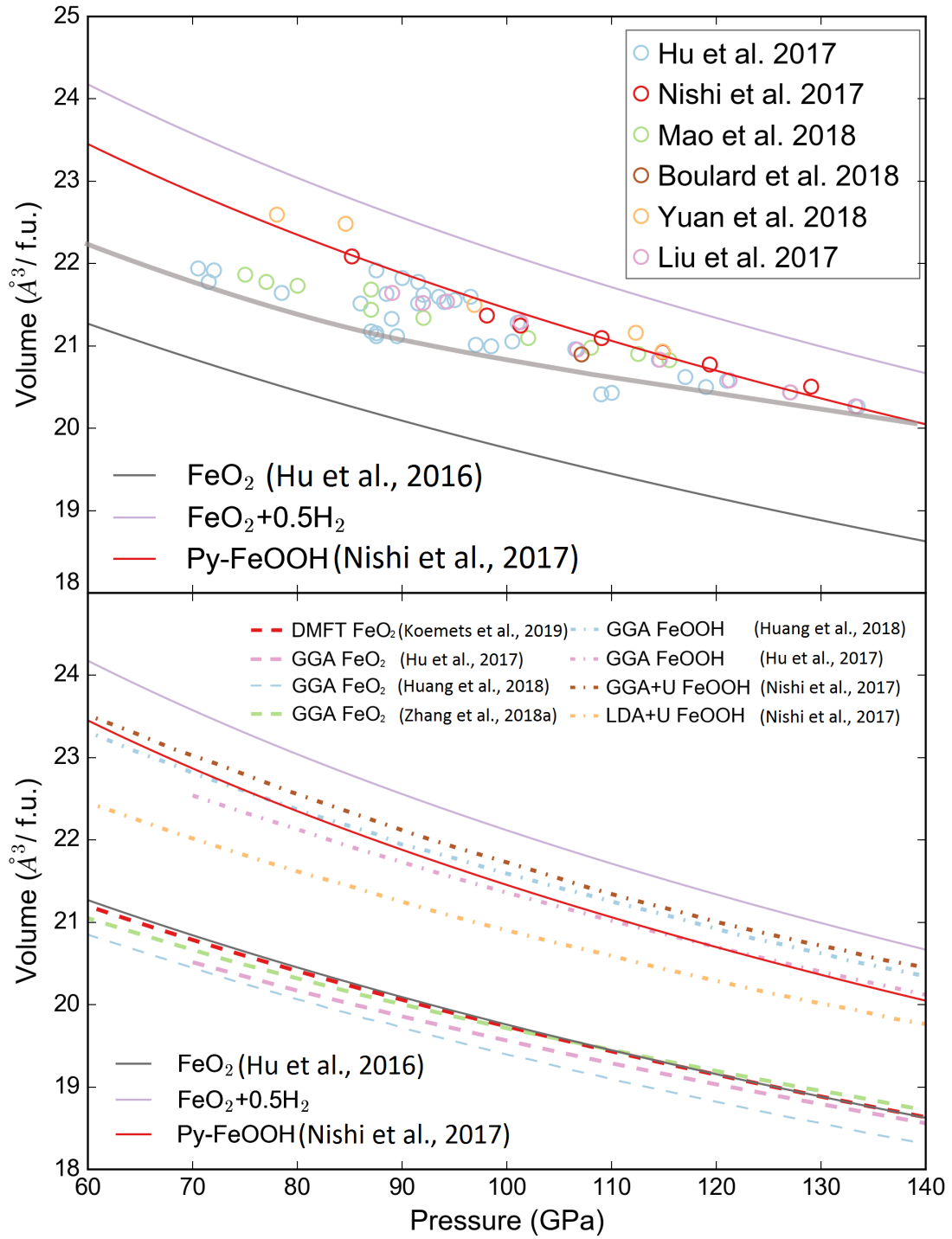
519 Table 1. Crystal data and structure refinement of polycrystalline Py- $\text{FeO}_2\text{H}_x$ . The  
520 powder refinement was implemented in GSAS, as in Fig. 3. The H position was not  
521 solved due to its weak charge density.

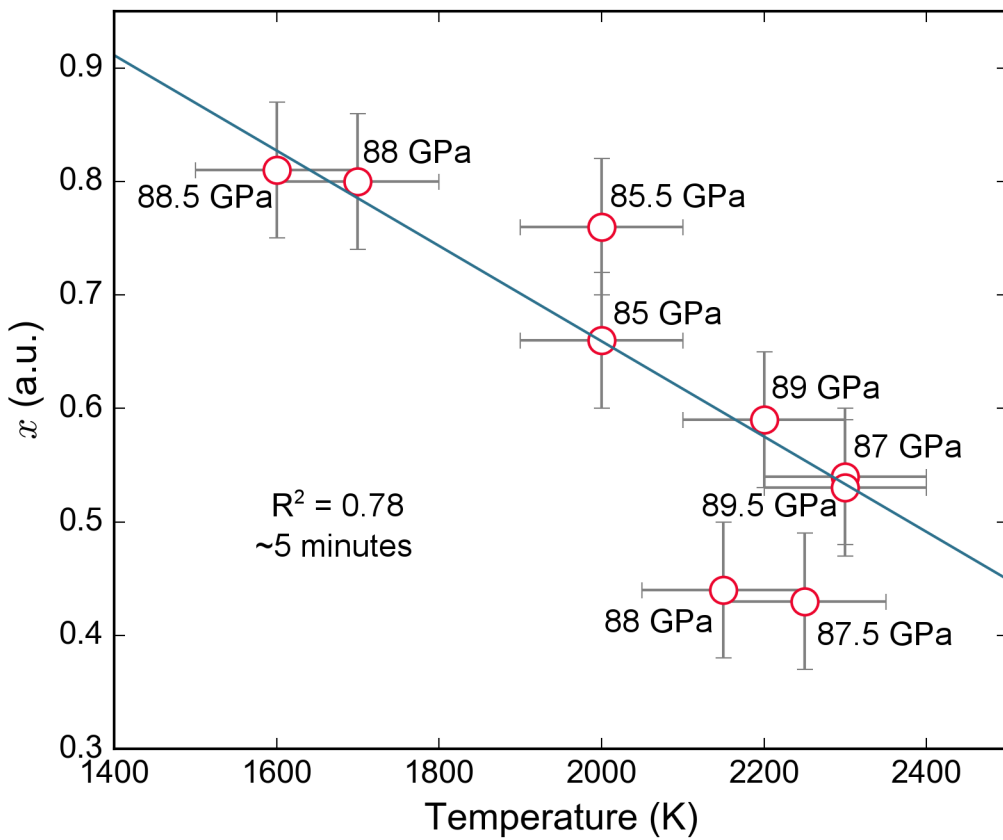
Journal Pre-proof	
Pressure	118(2) GPa
Temperature	293(2) K
Wavelength	0.4066 Å
Crystal system, space group	Cubic, $P\bar{a}\bar{3}$
Lattice parameters	4.3383 (1)
Atomic position	Fe: 0.0, 0.5, 0.5, Uiso 0.0309 O: 0.857(2), 0.357(2), 0.143(1), Uiso 0.0213
$R$ indices	$R_1 = 0.056$ , $wR_2 = 0.088$

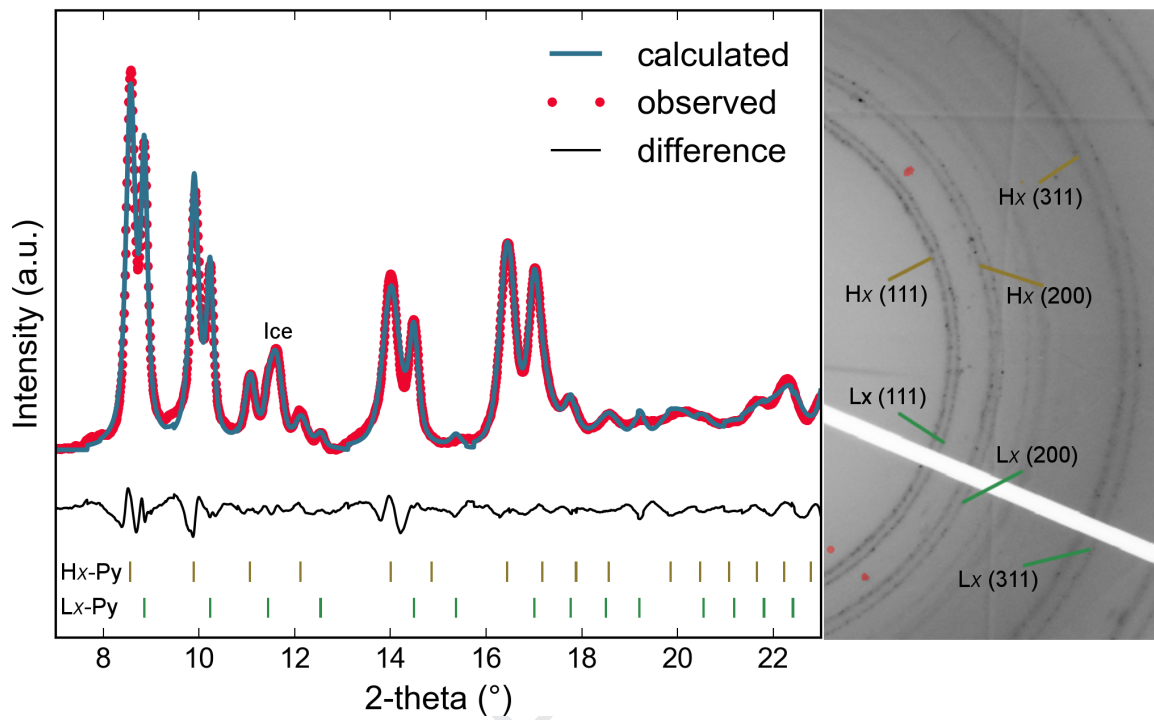


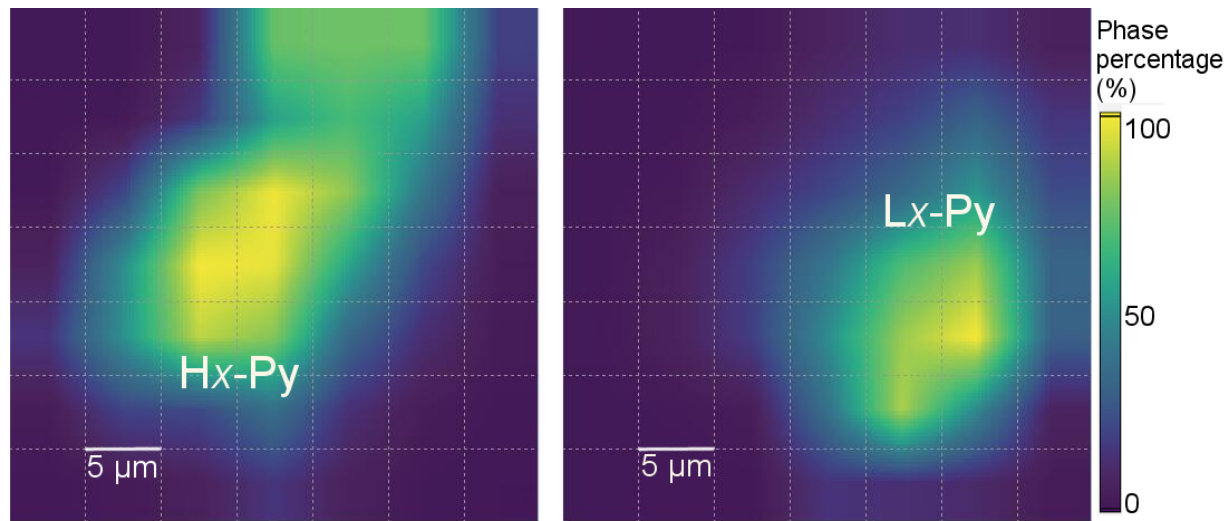


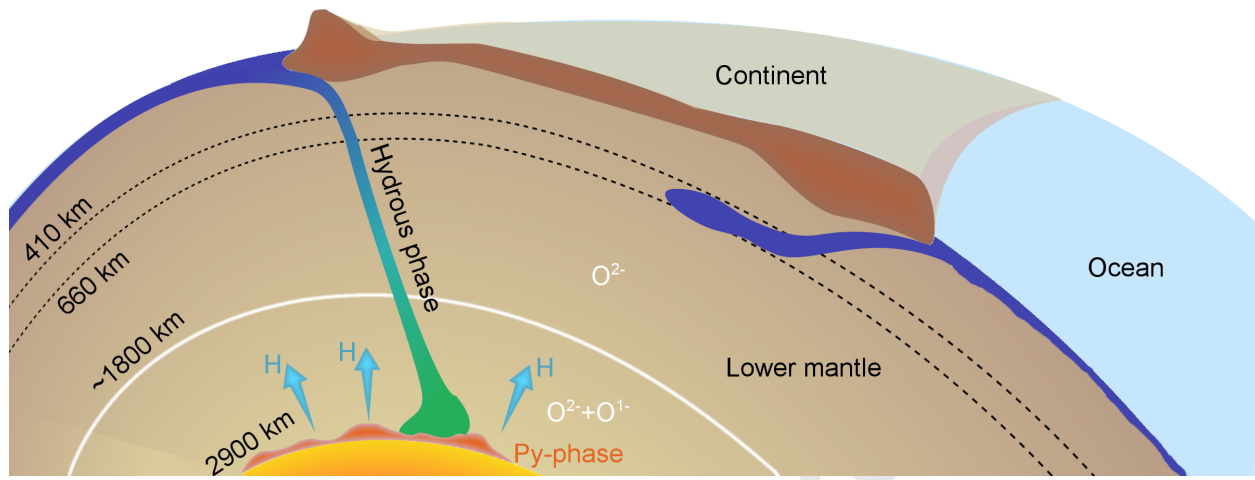


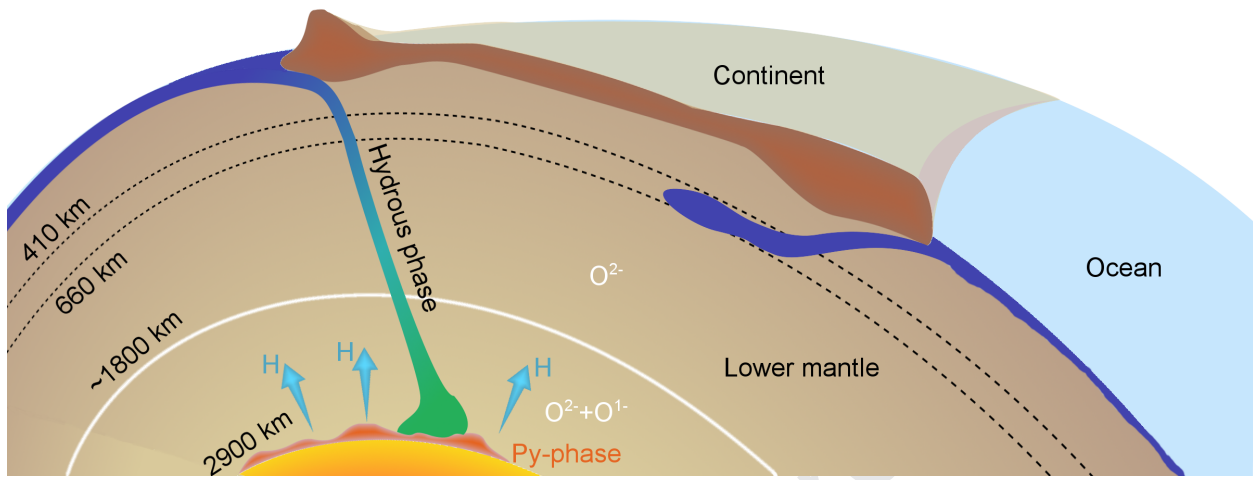












- Previous findings on the pyrite-type  $\text{FeO}_2\text{-FeO}_2\text{H}$  system are summarized and reviewed.
- The mobility of H in the  $\text{FeO}_2\text{-FeO}_2\text{H}$  system was characterized by x-ray diffraction in diamond anvil cell.
- The co-existence of pyrite-type phase with high-low concentrations of H was observed in a quickly decompressed sample.

**Declaration of interests**

The authors declare that they have no known competing financial interests or personal relationships that could have appeared to influence the work reported in this paper.

The authors declare the following financial interests/personal relationships which may be considered as potential competing interests:

